Wave Envelope and Infinite Element Schemes for Fan Noise Radiation from Turbofan Inlets

R.J. Astley* and W. Eversman†
University of Missouri-Rolla, Rolla, Missouri

Finite element models are presented for the calculation of radiated fan noise in the vicinity of turbofan inlets. The models involve the use of conventional axisymmetric finite elements in an inner region close to the inlet. The far field is represented by infinite elements or wave envelope elements. Theory and results are presented for the case with no mean flow. Comparisons of computed data with analytic solutions and measured values establish the utility of both the infinite element and wave envelope element schemes. The wave envelope scheme is shown to be effective also in the far field. Both schemes use meshes which are much sparser than would be required in conventional numerical discretizations and may be applied to real inlet configurations at modest computational cost.

Introduction

METHODS for predicting the modification of the acoustical field as it passes through the ducted (and usually acoustically treated) sections of a turbofan inlet are now well advanced and include wave envelope weighted residual schemes,[1] finite element (FE) schemes of various types, [2-4] and transient finite difference schemes,[5] all of which seem capable of handling the linear problem for realistic frequencies and Mach numbers.

The propagation of sound in the external region, which extends from the throat of the inlet to the far field, presents a more demanding computational problem and involves the imposition of radiation-type boundary conditions at an infinite (or at least distant) boundary. None of the numerical schemes currently developed for the ducted sections of inlets may be applied directly to the exterior region since the dimensionality of the linear matrix problem then required to resolve the relatively short wavelength disturbances typical of real inlets is prohibitively large.

A more subtle approach is therefore required, and a means must be found of confining the purely numerical portion of the solution within a relatively small computational domain close to the inlet itself. One such approach involves the application of boundary integral methods to the outer region, effectively modeling the outer field by a distribution of source functions over a control surface enclosing the inlet.[6] The effective impedance on this surface may then be matched iteratively to that of a conventional FE numerical solution in the inner region.

An alternative approach presented here involves the modification of the shape and weighting functions within a standard Galerkin FE scheme to accommodate the fine harmonic detail of the solution in the outer region. This is done either through the use of infinite elements, which impose an exaggerated exponential decay on the outer solution and consequently may only safely be used to predict the effect of the far field on the near field solution, or by the use of wave envelope elements that incorporate the gross features both of the asymptotic decay and of the harmonic variation in the outer portion of a finite but large computational domain. The wave envelope elements, which conceptually resemble those used for internal duct problems,[7] have the advantage of predicting reliable far-field values.

Infinite element and wave envelope radiation theories are presented in the current paper for the case with no mean flow. Results are presented which demonstrate the accuracy of the formulations proposed by a comparison of computed results with exact solutions for hyperboloid ducts and with experimental measurements for more realistic duct geometries. A second paper will discuss the case when flow is present.

Theory

Geometry and Governing Equations

The geometry of an idealized turbofan inlet is shown in Fig. 1. C_n denotes a rigid boundary and is formed, for the purposes of the present analysis, by the surface at the nacelle and a notional conical surface swept back at an angle θ_0 to the Z axis (if $\theta_0 = 180$ deg this surface becomes the centerline behind the inlet). C_f denotes a convenient plane within the nacelle at which it is assumed that a known ensemble of incident (i.e., traveling from left to right in Fig. 1), acoustic modes are present. C_f will be termed the "fan plane," although for cases where a uniform segment extends from the actual fan plane to the start of the expanding lip, C_f is conveniently moved forward to this point for reasons of computational economy.

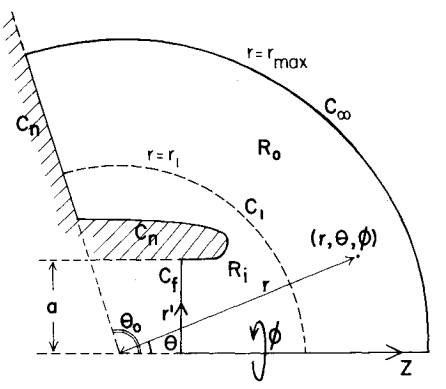

Fig. 1 Geometry of the inlet region.

Presented as Paper 83-0709 at the AIAA Eighth Aeroacoustics Conference, Atlanta, Ga., April 11-13, 1983; submitted June 3, 1983; revision received Jan. 12, 1984.

*Visiting Professor; currently Senior Lecturer, University of Canterbury, Christchurch, New Zealand.
†Professor. Associate Fellow AIAA.

The region in which a solution will be sought is then subdivided into inner and outer subregions R_i and R_o with an interface at the boundary C_f and an overall outer boundary at C_∞, as shown in Fig. 1. The acoustic potential in cylindrical coordinates is assumed to be of the form

$$\Phi^A(x,t) = \phi(r',z)e^{i\omega t}e^{-im\phi'} \tag{1}$$

the term $e^{-im\phi'}$ accounting for the presence of spinning acoustic modes generated by rotor-stator interaction. The integer m is termed the spinning or angular mode number. The field equation governing the acoustic velocity potential amplitude is then the Helmholtz equation

$$\nabla^2\phi + k^2\phi = 0 \tag{2}$$

where $k=\omega/c_0$ (c_0 denotes the ambient speed of sound). In the cylindrical coordinate system the appropriate form of the gradient operator is

$$\nabla = \frac{\partial}{\partial r'}\boldsymbol{e}_{r'} + \frac{\partial}{\partial z}\boldsymbol{e}_z - \frac{im}{r}\boldsymbol{e}_{\phi'} \tag{3}$$

where r', ϕ', z are cylindrical coordinates as indicated in Fig. 1, and $\boldsymbol{e}_{r'}$, $\boldsymbol{e}_{\phi'}$, $\boldsymbol{e}_z$ are the unit vectors in this system.

Boundary Conditions

The boundary condition on all rigid surfaces is that of zero normal particle velocity giving

$$\frac{\partial\phi}{\partial n} = 0 \text{ on } C_n \tag{4}$$

where n denotes a direction locally normal to the boundary, and directed out of the computational region.

On the fan plane, C_f, the appropriate boundary condition may be written

$$\phi = \sum_{i=1}^{\infty} A_i^+ f_i^+(r') + \sum_{i=1}^{\infty} A_i^- f_i^-(r') \tag{5}$$

and

$$\phi_z = \sum_{i=1}^{\infty} A_i^+ [-ik_i^+ A_i^+ f_i^+(r')] + \sum_{i=1}^{\infty} [-ik_i^- A_i^- f_i^- z(r')] \tag{6}$$

where the functions $f^\pm$ are solutions of the eigenvalue problem in the cylindrical duct section and represent incident and reflected waves propagating with wavenumbers $k_i^\pm$ (if $k_i^\pm$ is real the mode is "cut-on" and if complex "cut-off"). The coefficients A_i^+ are assumed known. The coefficients A_i^- must then be found during the course of the solution. Physically, boundary conditions (5) and (6) represent a matching of pressure and normal velocity between regions to the left and right of the fan plane, it being assumed that to the left of C_f a known set of incident modes is present.

The necessary boundary condition at the outer boundary of the solution region must simulate an anechoic surface. In the present analysis the outer boundary, denoted by C_∞, is a spherical surface at $r=r_{\max}$ (r, Θ, and ϕ are spherical polar coordinates as indicated in Fig. 1). It therefore can be assumed that if $r_{\max}$ is sufficiently large, the radiated field will behave locally as a plane wave propagating outward from the origin and normally incident on C_∞. This assumption yields

$$\frac{\partial\phi}{\partial r} = -ik\phi \text{ on } C_\infty \tag{7}$$

and is equivalent to the specification of a "ρc" impedance on C_∞. A useful physical interpretation of Eq. (7) and one which facilitates its extension to the case with mean flow is to regard it as a statement that at large distances from the inlet the sound field will behave as if it emanates from a single complex source located in the vicinity of the inlet.

The z axis of geometrical symmetry, which appears from Fig. 1 to constitute a boundary of the solution region, does not in fact do so, since the residual scheme described in the following section involves integration over the volume of revolution about the z axis. No boundary conditions need therefore be specified on the z axis.

The Residual Scheme

A general weighted residual scheme is now applied to the field equations and boundary conditions described in the preceding sections. An appropriate choice of the basis and weighting functions will then generate a variety of specific numerical schemes.

First, a trial function $\tilde{\phi}$ is assumed for the velocity potential amplitude ϕ. The trial function is formed as an expansion of known basis functions ψ_i ($i=1,\ldots n$) and unknown coefficients a_i giving

$$\tilde{\phi} = \sum_{i=1}^{n} a_i\psi_i \tag{8}$$

Substitution of $\tilde{\phi}$ into Eq. (2) yields residuals R and R_B in the field equations and boundary conditions

$$R = \nabla^2\tilde{\phi} + k^2\tilde{\phi}, \qquad R_B = \frac{d\tilde{\phi}}{dn} - \frac{d\tilde{\phi}}{dn} \tag{9}$$

for a specified velocity potential normal derivative $d\bar{\phi}/dn$ on the boundary.

These residuals are weighted by an appropriate set of weighting functions W_j ($j=1,\ldots n$) and integrated over the volume and surface boundaries. A combination of these integrated weighted residuals

$$\iiint_{\forall} W_j[\nabla^2\tilde{\phi} + k^2\tilde{\phi}]\,d\forall - \iint_S W_j\left[\frac{d\tilde{\phi}}{dn} - \frac{d\tilde{\phi}}{dn}\right]dS = 0 \qquad j=1,\ldots n \tag{10}$$

is then driven toward zero by determining appropriate coefficients a_i in the expansion of Eq. (8). An application of the divergence theorem, the observation that on C_n, $d\tilde{\phi}/dn = 0$; the observation that on C_f, $d\tilde{\phi}/dn$ is given by Eq. (6); and finally the observation that on C_∞, $d\tilde{\phi}/dn$ is given in terms of $\tilde{\phi}$ by Eq. (7), yields

$$\iiint_{\forall} [\nabla W_j \nabla\tilde{\phi} - k^2 W_j\tilde{\phi}]\,d\forall - \iint_{C_f} W_j\frac{d\tilde{\phi}}{dn}\,dS + ik\iint_{C_\infty} W_j\tilde{\phi}\,dS = 0 \qquad j=1,\ldots n \tag{11}$$

There still remains the boundary condition of Eq. (5) which is not included in the "natural boundary conditions" implemented above. There are several ways to approach this, including forming yet another weighted boundary residual, which produces an additional set of equations that relate the A_i^+ and A_i^- to the nodal velocity potential values on C_f. This adds additional equations, balancing the number of equations and unknowns (a_i, A_i^- are unknown, A_i^+ are known). This technique has been described in an earlier paper.[4] A second method expands the vector of nodal values of velocity potential on C_f in terms of the duct eigenfunctions on C_f. In the Galerkin scheme described in the next section the weighting functions W_j on C_f are also taken as the duct eigenfunctions. This method has been implied in principle previously,[3] where it is suggested that this procedure be carried out as a transformation of the assembled stiffness

matrix introducing the nodal expansion on C_f. In the present investigation a frontal solution technique has been developed requiring this transformation to be made at the element level inasmuch as assembly and solution are part of the same operation. While the frontal solution has now been implemented and the efficiency of the second approach proven, the results in this paper have been obtained using the first approach. In either case, the application of standard finite element "element stiffness matrix" calculations and "assembly" operations produces a set of linear algebraic equations of the form

$$\begin{bmatrix} K_{11} & K_{12} \\ K_{21} & K_{22} \end{bmatrix} \begin{Bmatrix} A^- \\ a \end{Bmatrix} = \begin{bmatrix} F_1 \\ F_2 \end{bmatrix} \{A^+\} \tag{12}$$

In the first treatment of C_f described above, the subvector $\{a\}$ includes both internal degrees of freedom and degrees of freedom on the boundary C_f. In the second case, $\{a\}$ includes only internal degrees of freedom. The second technique is therefore more efficient, but the savings in computations on the scale considered here is modest. The principal advantage of the second approach is that it is well suited for the frontal solution.

The above formulation is still general in the sense that it leaves open the choice both of the basis functions ψ_i and of the weightng functions W_i. Some particular choices of these functions are discussed in the following section.

Choice of Basis and Weighting Functions

The residual scheme described in the previous section was implemented with three different sets of basis and weighting functions. The most straightforward of the schemes involves the subdivision of both the inner and outer regions (R_i and R_o) into conventional finite elements. Nine noded isoparametric rectangles were used. A typical element is shown in Fig. 2a. The basis functions ψ_i are then defined by the global shape functions, $N_i(r',z)$, associated with node i of the discretization. The global shape functions are defined explicitly within each element by the appropriate element shape functions in the usual way. The coefficients a_i in the trial expansion then correspond to nodal values of ϕ. A standard Galerkin scheme may then be applied with the basis functions being used also as weighting functions.

The uniform duct eigenvectors and axial wavenumbers required for the evaluation of the boundary integrals on C_f can be determined analytically or numerically. In all of the schemes presented in this paper they were calculated numerically. In all of the schemes presented in this paper they were calculated numerically using a compatible finite element eigenvalue formulation on C_f, ensuring resolution in the eigenfunction expansion identical to that in the adjacent computational region. In the subsequent development of the frontal solution analytical eigenfunctions were used with no apparent change in the result.

The formulation described above will be termed the "conventional" FE scheme. It has several serious drawbacks when applied to inlet geometries at realistic frequencies. The most important of these is inherent in the choice of shape/basis functions. These are quadratic in the local coordinates ξ and η (see Fig. 2a) within each element. Several elements are therefore required to accurately represent a single wavelength variation of the solution in any direction. For realistic frequencies the typical far-field wavelength of the acoustic field may be an order of magnitude smaller than the diameter of the inlet and several orders of magnitude smaller than the overall dimension of the computational domain if the outer boundary is sufficiently distant to justify the assumption of a "ρc" impedance. The number of degrees of freedom then required for useful analysis becomes prohibitively large. It was in an attempt to overcome this basic problem that the "infinite element" and "wave envelope" (WE) schemes were developed. These are now described.

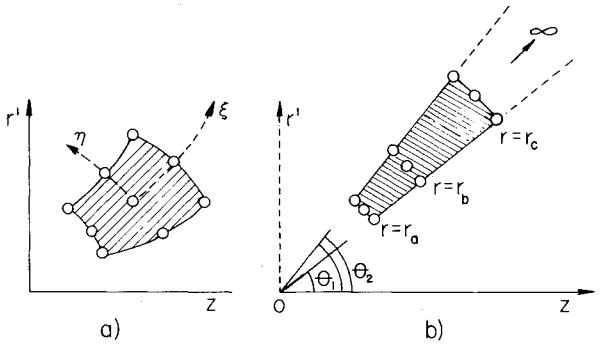

Fig. 2 Element topology: a) conventional element; b) infinitive/wave envelope element.

In the infinite element and WE schemes a different choice of weight and basis functions is made in the inner and outer computational regions. In the inner region, R_i, both ψ_i and W_i are chosen as in the conventional scheme. In the outer region, R_o, however, an attempt is made to include the gross features of the harmonic behavior of the solution within the basis functions themselves. The elements in the outer region are then required to resolve only the discrepancy between the actual solution and the implied harmonic and amplitude variations incorporated in the basis functions. Larger elements may therefore be chosen which extend over many wavelengths and a dramatic decrease in the overall dimensionality of the problem results.

The infinite element scheme, which derives from analogous two-dimensional water wave studies,[8] divides the outer region R_o into a single layer of elements. The outer boundary is moved to infinity and the elements are therefore of infinite extent. In the current analysis nine noded Lagrangian elements are used with the assumption that the conventional element shape functions for such an element may be extended within the infinite region enclosed by the broken lines in Fig. 2b. The mesh of infinite elements should be created so that the sides of the elements are surfaces of constant r and θ (r and θ being spherical polar coordinates as shown in Fig. 1). The basis and weight functions corresponding to any node i within the outer region are then defined by

$$W_i = \psi_i = N_i(r,\theta)\exp[-(ik+1/L)(r-r_i)] \tag{13}$$

The function $N_i(r,\theta)$ in the above expression denotes the conventional global shape function. The exponential factor includes an outward propagating wave-like factor, of wavenumber k, and an exponential spatial decay of length scale L. The factor $(r-r_i)$ in the exponential argument ensures that $\psi_i \equiv 1$ at node i (r_i denotes the polar radial coordinate of node i) and hence preserves the significance of the coefficients a_i as nodal values of $\tilde{\phi}$.

Element integrations involve oscillatory integrands and conventional Gaussian quadrature cannot be used. Reference 8 can be consulted for details.

The choice of the length scale L which occurs in the definition of W_i and ψ_i is arbitrary to the extent that any value of L which approximately represents the amplitude decay in the vicinity of R_i will give a reasonable inner solution.[8,9] It is one of the problems of infinite element solutions, however, that whatever the rate of exponential decay chosen, it will inevitably fail to represent the far-field solution which, for three-dimensional problems, is characterized by reciprocal decay. This deficiency is remedied in the WE approach.

The WE scheme is initially similar to the infinite element formulation in that the weight and basis functions are once again identified with the global shape functions within the inner region R_i. The outer region, however, is subdivided into one or more layers of large but finite elements, oriented on

lines of constant r and θ. The topology of a typical WE element is indicated by the shaded element of Fig. 2b. C_∞ is retained as an outer finite boundary. The basis functons ψ_i in the outer region were originally defined by

$$\psi_i = N_i(r,\theta)\,(r_i/r)\exp[-ik(r-r_i)] \tag{14}$$

where $N_i(r,\theta)$ denotes the conventional global shape function associated with node i. The basis functions so defined incorporate reciprocal decay and a wave-like variation corresponding to a locally outward traveling wave. They also have the property that $\psi_i \equiv 1$ at node i and the coefficients a_i once more retain their significance as nodal values of $\tilde{\phi}$. The weight functions for the WE scheme are chosen to be the complex conjugates of the basis functions, i.e.,

$$W_i = N_i(r,\theta)\,(r_i/r)\exp[+ik(r-r_i)] \tag{15}$$

Since the conventional shape functions are real, this only affects the harmonic factor but has the attractive consequence of causing the exponential terms within the integrands of Eq. (11), which arise from products of W_i, ψ_i, and their derivatives, to cancel identically. Conventional Gauss-Legendre numerical integration may therefore be used even though each element extends over many wavelength variations of W_j and ψ_i. For the current analysis, three-point integration was used in the r and θ directions.

Recent experimentation suggests that the (r_i/r) decay is not necessary and that little change in results is observed if it is deleted, simplifying the element calculations.

Results

Four sets of results will be presented. Initially the performance of the three numerical schemes (conventional, WE, and infinite element) is assessed by a comparison of computed and analytic solutions for spinning mode propagation in a hyperboloid expansion. A comparison then follows between computed and experimental results for two inlet geometries at relatively low frequencies. Finally, a comparison of computed and measured directivity patterns is presented for a high-frequency test inlet. All results are presented in terms of acoustic pressure amplitude p or sound pressure level (SPL). In the numerical schemes p is related to the computed velocity potential amplitude by $p = \rho_0 i\omega\tilde{\phi}$.

Comparison with Analytic Results

An analytic solution incorporating many of the features of real inlets (e.g., spinning mode propagation, modal mixing, exit reflections) is to be found in an exact solution[10] for sound propagation through a family of hyperboloid ducts. The geometry for which these solutions hold is shown in Fig. 3 and consists of a hyperbolic expansion that develops from a cylindrical section and tends asymptotically to a conical surface of cone angle θ_0. Results were calculated using all three numerical schemes for the particular case $\theta_0 = 70$ deg and $\phi = 8$. The frequency range for which results were obtained includes the cut-on frequency of the first two modes in the cylindrical section (at the inlet section AB of Fig. 3) and corresponds to values of the nondimensional parameter ka in the range $9.0 < ka < 15.0$. Both the computed and analytic solutions are presented for single incident modes. Contour plots of the absolute value of acoustic pressure were used as a convenient representation of the numerical solutions. Such plots are shown in Fig. 4 for the case $ka = 11$ with mode 1 incident (all other modes being cut off at this frequency). Contours are plotted for the conventional and WE schemes and are superimposed on a representation of the WE mesh which was used to obtain the latter results. The WE mesh for this problem comprised a fine mesh of conventional elements in the region $r < r_l (= 1.6a)$ with four layers of WE elements in the outer region $r_l < r < r_{\max} (= 4a)$. The conventional results plotted in Fig. 4 were obtained using a mesh with fine resolution over the entire region approximately equivalent to the resolution in the inner region of the WE mesh. Inset in Fig. 4 (and in all similar figures to follow) is a representation of the characteristic far-field wavelength of the problem $(= 2\pi/k)$. Within the conventional inner region an axial mesh resolution of approximately five elements per wavelength is used. Within the WE region this density is decreased to less than one element per wavelength with little perceptible effect on the resulting solution.

Analogous infinite element results are presented in Fig. 5a, which shows pressure contours in the inner region obtained by replacing the WE elements of Fig. 4 by a single layer of infinite elements. These contours are in fact in very close agreement with those of Fig. 4 and are compared in Fig. 5b with the equivalent contours obtained by decreasing the dimensionality of the conventional scheme by reducing the value of $r_{\max}$ to that of r_l in the WE scheme (i.e., $1.6a$). The solutions of Figs. 5a and 5b therefore represent the same computational effort. It is clear, however, that in Fig. 5b significant spurious reflections have been introduced as a result of the C_∞ boundary being no longer sufficiently distant to justify the "ρc" impedance. Such effects are not apparent in the infinite element or WE schemes.

The correspondence of all three schemes to the exact solution is demonstrated in Figs. 6-8. Figures 6 and 7 show analytic and computed values of the reflection coefficients R_{11} and R_{12} at the fan plane (R_{ij} being defined to be the reflection coefficient in mode j with mode i incident) and give a measure of the accuracy of the computed solution in the near field. Figure 8 shows computed and exact values of the far-field directivity function $\phi(\theta)$ (defined by $p(r,\theta) \sim$

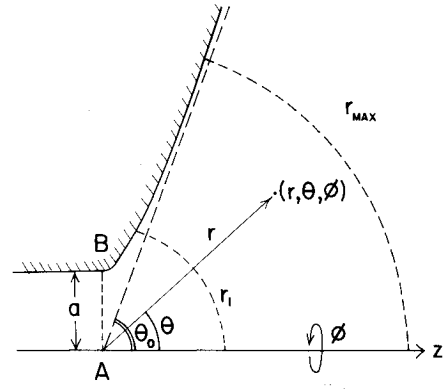

Fig. 3 Hyperbolic horn geometry.

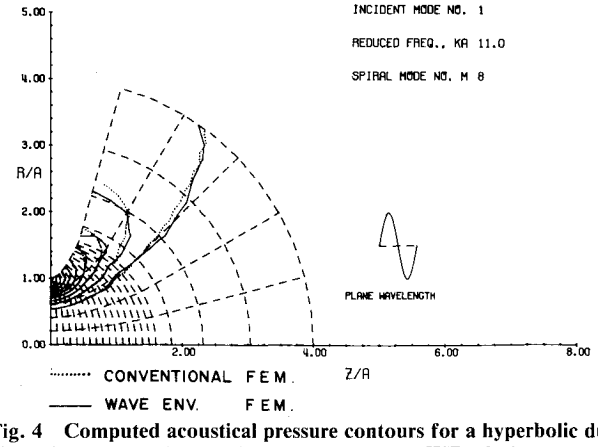

Fig. 4 Computed acoustical pressure contours for a hyperbolic duct ($\theta_0 = 70$ deg, $ka = 11$, $m_\phi = 8$), conventional and WE solutions.

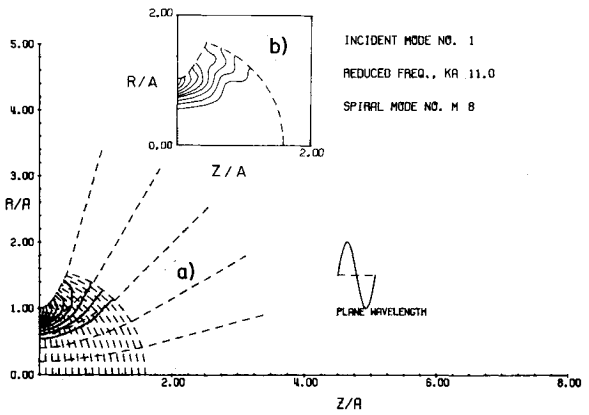

Fig. 5 Computed acoustical pressure contours for a hyperbolic duct ($\theta_0 = 70$ deg, $ka = 11$, $m_\theta = 8$), infinite element and conventional solutions.

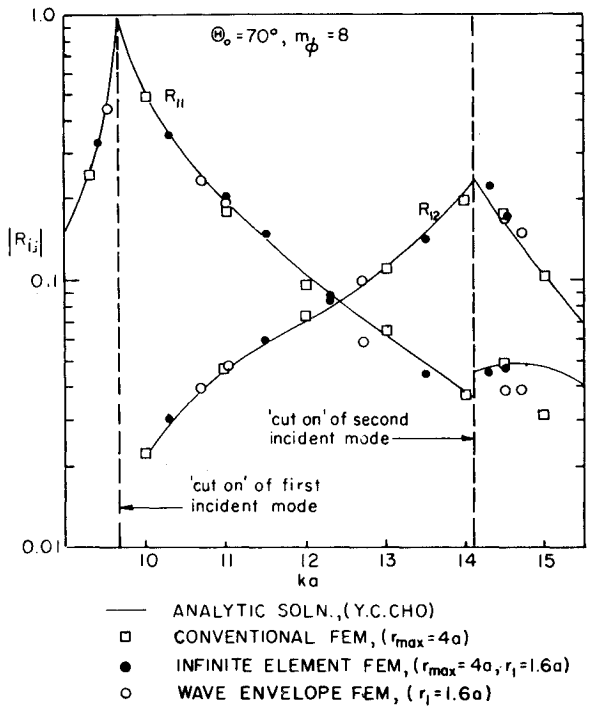

Fig. 6 Computed and exact reflection coefficients for a hyperbolic duct ($\theta_0 = 70$ deg, $m_\phi = 8$), absolute value.

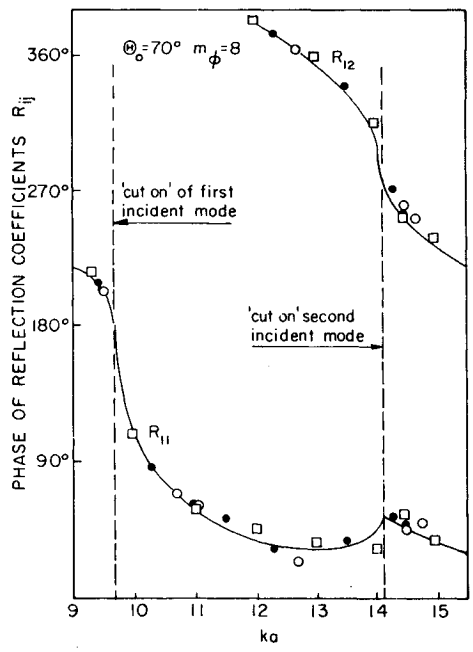

Fig. 7 Computed and exact reflection coefficients for a hyperbolic duct ($\theta_0 = 70$ deg, $m_\phi = 8$), phase.

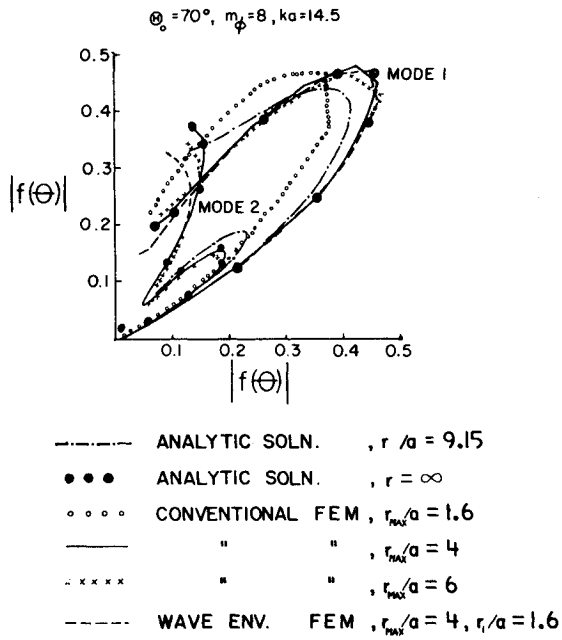

Fig. 8 Computed and exact directivity patterns for a hyperbolic duct ($\theta_0 = 70$ deg, $ka = 14.5$, $m_\phi = 8$).

$\phi(\theta)/r$ as $r \to \infty$) plotted for modes 1 and 2 incident at a frequency corresponding to $ka = 14.5$. Discrepancies do appear in Figs. 6 and 7 as R_{11} and R_{12} become small. These are due to a general loss in accuracy as the reflected portion of the solution becomes small compared with the remainder of the acoustical field and are also attributable to the effects of small spurious reflections at the ρc boundary. These become a significant portion of the reflected field if R_{11} or R_{12} is sufficiently small. It is noticeable in this regard that the infinite element scheme appears to be the most accurate of the three formulations in predicting the reflection coefficients, partially as a consequence of its implicit removal of the ρc termination to infinity and avoidance thereby of any spurious reflections. The infinite element scheme does not, however, predict the far field, and the comparisons of Fig. 8 therefore include only conventional, WE, and analytical solutions. Of interest in Fig. 8 is the effect of varying r_{max} in the conventional scheme. For $r_{max} = 1.6a$ the computed directivity function is significantly distorted by near-field effects. For larger values of r_{max} ($4a$ and $6a$), however, the conventional and WE schemes are in excellent agreement with the asymptotic analytic far-field values. A somewhat peculiar feature of Fig. 8 is the analytic solution of $r = 9.15a$ which does not appear to converge to the asymptotic solution as rapidly as the numerical solutions would indicate. It has been suggested that some of the near-field effects are being effectively filtered out of the numerical solution by the imposition of the asymptotic "ρc" boundary condition at a finite boundary. If so, this is a fortuitous effect in the context of far-field directivity calculations.

Comparison with Experiment: Low Frequency

A comparison of WE and experimental results is now presented for two inlet geometries. The first of these is an

elliptical "flight inlet" for which experimental data are obtained in the NASA Langley spinning mode test facility.[11] Although the measured data are for relatively low frequencies and angular mode numbers ($m_\phi = 1$), they are particularly valuable for comparison purposes since they include measurements both of the modal composition at the fan plane and of the far-field sound pressure levels. The far-field results may therefore be normalized with respect to the incident amplitudes and a comparison made on the basis of the magnitude *and* directivity of the far-field SPL. Other data currently available require more arbitrary normalization of the far-field measurements. A comparison of computed WE and measured data is presented for two frequencies corresponding to $ka = 2.66$ and 3.2. Computed contours of sound pressure level (SPL) for $ka = 2.66$ are shown in Fig. 9. They are plotted at 4-dB increments and are superimposed on a representation of the WE mesh, the outer region of which contains eight layers of WE elements and extends from $r_1 = 3a$ to $r_{max} = 10a$. The physical lip geometry is indicated by the shaded region near the fan plane C_f. A rear (and fictitious) computational boundary is placed 135 deg behind the centerline. A comparison of measured and computed far-field SPL values is shown in Fig. 10. For this far-field comparison, as for all that follow, the computed solution at C_∞ (in this case at $r = 10a$) is assumed to determine the "asymptotic" far-field directivity function $f(\theta)$. This is then used to determine actual pressure levels at specific measured radii ($r = 20.3a$ in this case). It must be assumed, of course, that the asymptotic solution holds at the distances involved, an assumption which is easily checked by increasing r_{max} in the computed solution and noting any variation in $f(\theta)$. In this case WE solutions were obtained for $r_{max} = 20a$ and $30a$ with little perceptible alteration to the computed SPL values of Fig. 10 to the scale shown. Since comparisons are being made effectively on the basis of asymptotic behavior, some latitude is also consistently permitted in the choice of the computational origin. In this case, the computational origin is at the fan plane C_f of Fig. 10, whereas the experimental origin is at a reference plane C_{ref} also shown. Asymptotically this difference will not affect the far-field directivity and no adjustment of data was therefore considered necessary.

From Fig. 10 it is clear that excellent agreement exists between the measured and predicted data, certainly in the forward quadrant ($\theta < 90$ deg). The presence of the rear computational boundary causes some reflection (clearly seen in Fig. 9) but does not affect the forward directivity pattern if the boundary is sufficiently oblique to the inlet. In general, it has been found (after numerical experimentation with a number of inlets) that as long as the computational boundary is approximately 90 deg to the rear of the principal radiation lobe its effect on forward radiation is sufficiently small to be neglected.

The close correspondence between theory and experiment evident in Fig. 10 is also apparent in a comparison of measured and calculated reflection coefficients. Referenced to C_f (of Fig. 10) these are

measured: 0.351/32.5 deg (magnitude/phase)

calculated: 0.346/21.5 deg (magnitude/phase)

A second comparison of far-field SPL values for a slightly higher frequency, $ka = 3.20$, is shown in Fig. 11. Once again, the correspondence between measured and calculated data is generally good. The reflection coefficients in this case are 0.196/32 deg (measured) and 0.157/−25 deg (calculated), representing a reasonable agreement of magnitude but a somewhat perplexing phase difference.

The second set of low-frequency test data against which the numerical schemes were assessed was that for a "bellmouth" inlet, also tested at the NASA Langley spinning mode facility.[12] The data are somewhat older and do not include normalization of the far-field directivity measurements with respect to the incident mode amplitudes. The measured and predicted SPL curves are therefore normalized with respect to their largest values. A typical computed WE solution with $r_{max} = 10a$ is shown in Fig. 12.

Computed SPL contours (at 4 dB increments) are shown for the case $ka = 5.81$ and $m_\phi = 4$. The geometry of the actual inlet is indicated by a heavy solid line. Once again a rigid boundary is imposed at $\theta_0 = 135$ deg. Measured and predicted far-field

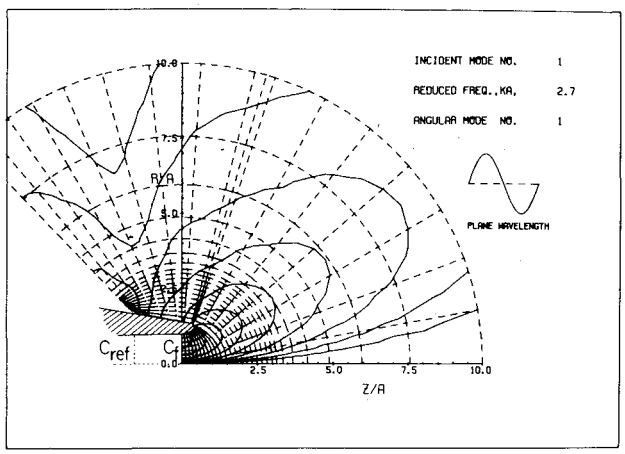

Fig. 9 Computed acoustical pressure contours for a flight inlet, ($m_\phi = 1$, $ka = 2.66$), WE solution.

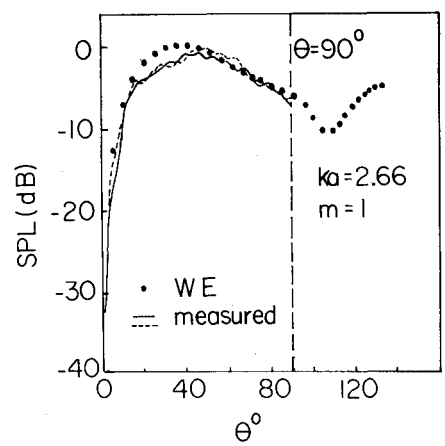

Fig. 10 Computed and measured SPL directivity for a flight inlet ($m_\phi = 1$, $ka = 2.66$).

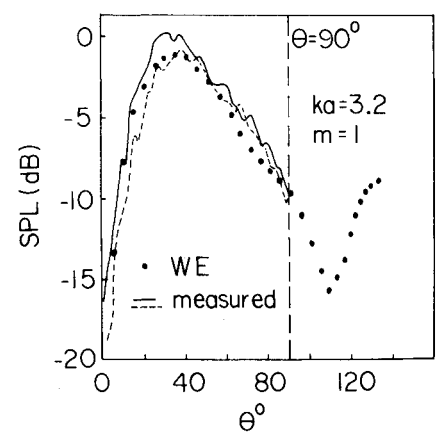

Fig. 11 Computed and measured SPL directivity for a flight inlet ($m_\phi = 1$, $ka = 3.2$).

SPL curves for this case are shown in Fig. 13. Given the considerable asymmetry in the measured data, agreement is generally good in the forward quadrant. The reflections associated with the rear boundary are no longer accurately resolved but again do not impinge on the forward radiation pattern. A comparison of the absolute value of the measured and predicted reflection coefficients for this inlet is shown in Fig. 14. Measured, WE, and conventional results are shown for $m_\phi = 2$ and 4. The meshes used for the WE and conventional results are somewhat coarser than that shown in Fig. 12. Comparison between theory and experiment is generally good, and it is interesting to note that for the conventional solutions (which were obtained with $r_{max} = 5a$) reflections at the ρc boundary are clearly discernible as R_{11} becomes small. Also shown in Fig. 14 is an approximate curve obtained by matching a hyperboloid expansion to the inner portion of the inlet lip and applying Cho's solution.[10] As one might expect, the correct geometrical representation of the inlet geometry, inherent in the numerical schemes, brings the predicted results into better agreement with measured data.

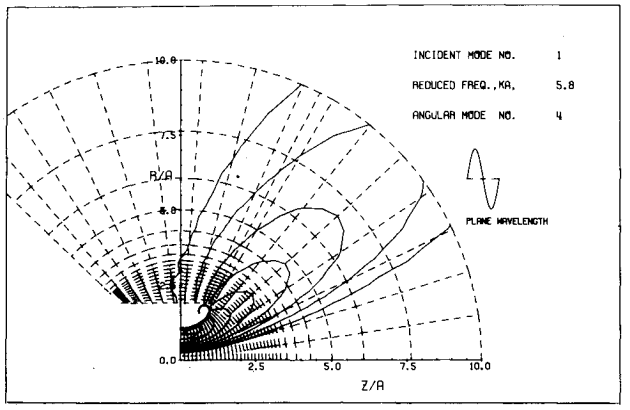

Fig. 12 Computed acoustical pressure contours for a bellmouth inlet ($m_\phi = 4$, $ka = 5.81$), WE solution.

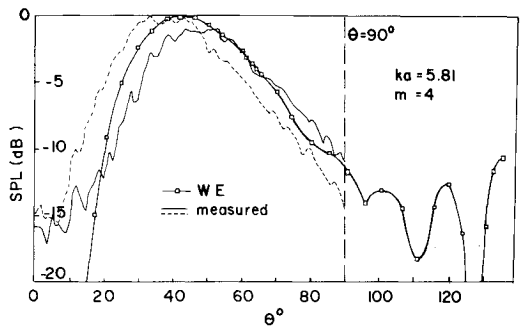

Fig. 13 Measured and computed SPL directivity for a bellmouth inlet ($m_\phi = 4$, $ka = 5.81$).

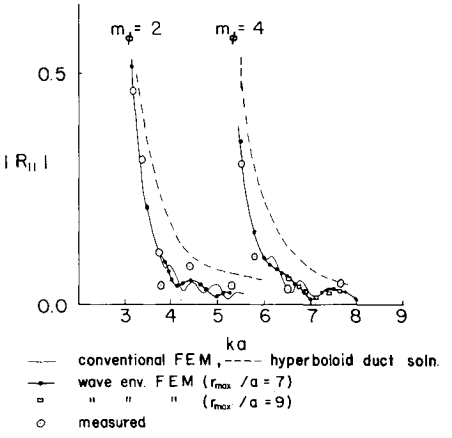

Fig. 14 Measured and computed reflection coefficients (absolute value) for a bellmouth inlet ($m_\phi = 2$ and $m_\phi = 4$).

Comparison with Experiment: High Frequency

Finally a comparison is presented between theory and experiment for an inlet at a (more or less) realistic frequency and angular mode number. The experimental data for this comparison were obtained from tests conducted at the NASA Lewis vertical lift facility.[6] A JT15D turbofan engine with a rotor-stator arrangement of 41 stator rods and 28 rotor blades was used to produce spinning modes of angular mode number 13. The cut-on frequency for this configuration coresponds to a value of ka in the vicinity of 15.0. The measured data currently available comprise far-field SPL measurements normalized to 100 dB at $\theta = 60$ deg. Data are only available at this time for the case $ka = 15.4$, corresponding to a frequency slightly above cut-on of the first mode. All other modes are strongly cut off. Computed SPL contours (at 4-dB increments) for $ka = 15.4$ and $m_\theta = 10a$. The mesh used for the calculation of these results is indicated by the broken lines in Fig. 15. The far-field SPL values predicted by this solution are plotted in Fig. 16 and compared with measured values (computed and measured results are both normalized to 100 dB at $\theta = 60$ deg). Also shown in Fig. 16 are WE results for a more extensive mesh with $r_{max} = 30a$ demonstrating a large degree of convergence of the WE far-field results to an

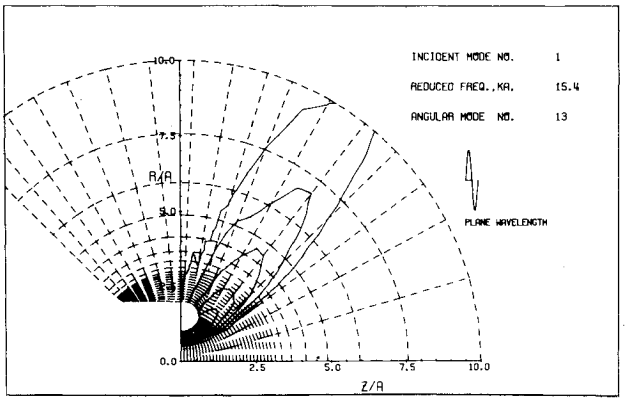

Fig. 15 Computed acoustical pressure contours for JT15D inlet ($m_\phi = 13$, $ka = 15.4$), WE solution.

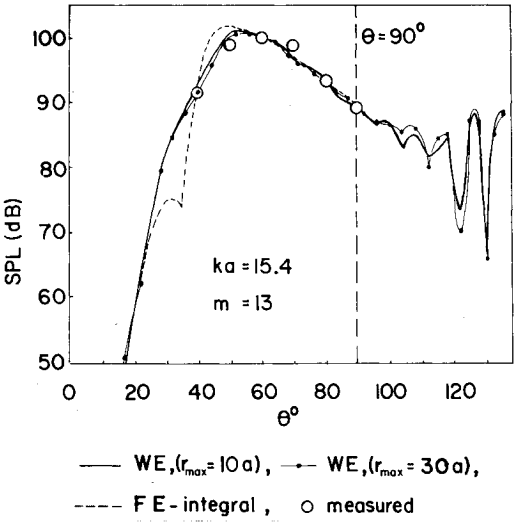

Fig. 16 Measured and computed SPL directivity for JT15D inlet ($m_\phi = 13$, $ka = 15.4$).

asymptotic limit. Results from the finite element integral theory[6] for the same problem are also plotted. The measured data are admittedly somewhat sparse, but the correspondence between predicted WE results and measured values appears to be good in the forward quadrant. The boundary at $\theta_0 = 134$ deg produces spurious reflections that are not well resolved by the numerical solution but that again do not affect the solution greatly in the regions at significant forward radiation.

Conclusions and General Discussion

Of the three schemes presented in this paper (conventional, wave envelope, and infinite element) it is clear that the latter two are capable of producing useful results for fan noise radiation at realistic frequencies and angular mode numbers. The conventional scheme is disqualified in this regard by virtue of its inherent dimensionality requirements at high frequencies. Comparisons with analytic results indicate that both the WE and infinite element schemes are as successful as the conventional scheme in predicting near-field effects and do so at greatly decreased computational cost. The WE scheme, moreover, appears capable of predicting accurate far-field behavior with much sparser meshes than would be required for a conventional approach and has been shown to give results that are generally in good agreement with experiment. It is worth noting that, even for the high-frequency test case of Figs. 15 and 16, the computational requirements of the WE program are relatively modest (approximately 100 s of CPU time and 0.85 megabyte storage on an AMDAHL 470V18 with double precision complex arithmetic throughout) and its application to even higher frequency cases, when data are available, should present few practical difficulties.

One important effect omitted from the present analysis is that of mean flow. The inclusion of mean flow in the inner region of the current numerical scheme requires only algebraic modification in that the original residual scheme must be reformulated with the full field equation in place of Eq. (2). In the outer region, however, some conceptual modifications are required when nonzero mean flow exists at C_∞ (as would occur in flight, for example). Asymptotically the inlet would then behave as a stationary complex source in a mean flow and the asymptotic behavior incorporated in the current WE and infinite element schemes should be modified accordingly. The term e^{-ikr}, extracted from the solution in both cases and placed in the shape functions, should be replaced by the term $e^{-ik\gamma(x)}$, where $\gamma(x)$ is the phase of the radiated field due to a simple source in the mean flow. For uniform mean flow in the z direction with Mach number M, $\gamma(x)$ is given by

$$\gamma(x) = (1/\beta^2)\,[Mz + (z^2 + \beta^2 r^2)^{1/2}]$$

where $\beta = \sqrt{1-M^2}$ The extension of the current WE or infinite element schemes to the case with flow is accomplished by a reformulation of the outer mesh so that the infinite and wave envelope elements are bounded by lines of equal phase and by ray paths (in the case of no mean flow, lines of constant θ and lines of constant r are such lines).

In the present formulation, when flow is absent, a boundary condition on the inlet inner surface corresponding to a point reacting liner is easily implemented via a boundary integral. The entire procedure is completely compatible with the formulation discussed here. When flow is present and the slip flow boundary condition is employed a complication is introduced by the presence of the pressure spatial derivative in the direction tangent to the wall. Since we are working with a velocity potential formulation the boundary condition involves a second derivative of the potential. This dictates the use of elements with higher order continuity, at least adjacent to the lined section. Other approaches include the use of integration by parts on the boundary to reduce the continuity requirement and a reformulation of the problem in terms of potential and pressure with the same elements used in the no-flow case.

A final point to be mentioned concerns the choice of the boundary between the conventional elements and the wave envelope elements. The distance to this boundary, denoted by r_1, is problem dependent. Both the inlet geometry and acoustic wavelength affect the choice of r_1. For conventional geometries, r_1 should be at least 3-3.5 duct diameters from the inlet. However, for high frequencies, the required r_1 increases. The reason is that in the wave envelope region the assumption is made that the radiation is nearly that of a source representing the inlet, any variation being absorbed in the shape functions. How nearly this assumption is satisfied at given r_1 depends on the compactness of the source. Hence, if the wavelength is short the source appears less compact and r_1 should exceed 3-3.5. If r_1 is chosen too close, standing waves become apparent in the inner region. The far-field directivity does not appear to be radically affected by a modest underestimation of r_1.

Acknowledgment

The work reported in this paper was supported by the NASA Langley Research Center under Grant NAG-1-198.

References

[1] Nayfeh, A.H., Shaker, B.S., and Kaiser, J.E., "Transmission of Sound Through Non-Uniform Circular Ducts with Compressible Mean Flow," *AIAA Journal,* Vol. 18, May 1980, pp. 515-525.

[2] Sigman, R.K., Majjigi, R.K., and Zinn, B.T., "Determination of Turbofan Inlet Acoustics Using Finite Elements," *AIAA Journal,* Vol. 16, Nov. 1978, pp. 1139-1145.

[3] Astley, R.J. and Eversman, W., "Acoustic Transmission in Lined Ducts with Flow, Part 2: The Finite Element Method," *Journal of Sound and Vibration,* Vol. 74, 1981, pp. 103-121.

[4] Astley, R.J. and Eversman, W., "A Finite Element Method for Transmission in Nonuniform Ducts Without Flow: Comparison with the Method of Weighted Residuals," *Journal of Sound and Vibration,* Vol. 57, No. 3, 1978, pp. 367-388.

[5] Baumeister, K.J., "Time Dependent Difference Theory for Noise Propagation in a Two-Dimensional Duct," *AIAA Journal,* Vol. 18, Dec. 1980, pp. 1470-1476.

[6] Baumeister, K. J. and Horowitz, S. J., "Finite Element—Integral Simulation of Static and Flight Fan Noise Radiation from the JT15D Turbofan Engine," NASA TM 82936, Nov. 1982.

[7] Astley, R.J. and Eversman, W., "A Note on the Utility of a Wave Envelope Approach in Finite Element Duct Transmission Studies," *Journal of Sound and Vibration,* Vol. 76, June 1981, pp. 595-601.

[8] Bettess, P. and Zienkiewicz, O.C., "Diffraction and Refraction of Surface Waves Using Finite and Infinite Elements," *International Journal for Numerical Methods in Engineering,* Vol. 11, 1977, pp. 1271-1290.

[9] Astley, R.J. and Eversman, W., "Finite Element Formulations for Acoustical Radiation," *Journal of Sound and Vibration,* Vol. 88, No. 1, 1983, pp. 47-64.

[10] Cho, Y.C., "Rigorous Solutions for Sound Radiation from Circular Ducts with Hyperbolic Horns or Infinite Plane Baffle," *Journal of Sound and Vibration,* Vol. 69, No. 3, 1980, pp. 405-425.

[11] Silcox, R.J., "Experimental Investigation of Geometry and Flow Effects on Acoustic Radiation from Duct Inlets," AIAA Paper 83-0173, April, 1983.

[12] Ville, J.M. and Silcox, R.F., "Experimental Investigation of the Radiation from an Unflanged Duct and a Bellmouth, Including the Flow Effect," NASA TP 1697, 1980.